Mon. Not. R. Astron. Soc. **000**, 1–?? (1994) Printed 2 February 2008 (MN LATEX style file v2.2)

Chemical evolution of the M82 B fossil starburst

Geneviève Parmentier[1], Richard de Grijs[2], and Gerry Gilmore[2]
[1] *Institute of Astrophysics and Geophysics, Université de Liège, Sart-Tilman (B5c), 4000 Liège, Belgium*
[2] *Institute of Astronomy, Madingley Road, Cambridge, CB3 0HA*

arXiv:astro-ph/0302321v1 17 Feb 2003

Accepted . Received ; in original form

ABSTRACT
M82 B is an old starburst site located in the eastern part of the M82 disc. We derive the distributions of age and metallicity of the star clusters located in this region of M82 by using theoretical evolutionary population synthesis models. Our analysis is based on the comparison of the $BVIJ$ photometry obtained by de Grijs et al. (2001) with the colours of single-generation stellar populations. We show that M82 B went through a chemical enrichment phase up to super-solar metallicities around the time of the last close encounter between M82 and its large neighbour galaxy M81. We date and confirm the event triggering the enhanced cluster formation at about 1 Gyr ago. At almost the same time an additional, distinct subpopulation of metal-poor clusters formed in the part of M82 B nearest to the galactic centre. The formation of these peculiar clusters may be related to infall of circumgalactic gas onto M82 B.

Key words: galaxies: individual: M82 - galaxies: starburst - galaxies: star clusters.

1 INTRODUCTION

Stellar clusters constitute unique laboratories for studying past and present star formation episodes in galaxies. Their ages and metallicities provide valuable insights into the star formation history as well as the chemical evolution of the host galaxy. Star clusters are especially important for understanding the history of galaxies beyond the Local Group. These galaxies are too far away for their stars to be easily resolved individually, so that most of the information is derived from the integrated properties of star clusters, especially of the brightest, most massive ones.

This field has seen impressive developments during the past decade thanks to the advent of the *Hubble Space Telescope* (*HST*) and large ground-based telescopes. One of the main contributions to date of the refurbished *HST* is the discovery of young clusters with typical globular cluster (GC) masses in galaxies beyond the Local Group. While the formation of GCs was previously thought to be restricted to the early history of the Universe, the discovery of such candidate young GCs shows that the formation of massive stellar clusters, with masses $m > 10^4 - 10^5\,M_\odot$, continues today.

Young and/or intermediate age massive clusters, sometimes referred to as "super star clusters" (SSCs) by virtue of their high luminosities, have been detected mostly in interacting and merging galaxies. The accumulation of such observations (e.g. Holtzman et al. 1996, Zhang, Fall & Whitmore 2001, de Grijs et al. 2001) have highlighted a clear causal link between strong starbursts on the one hand and tidal interactions (e.g. the starburst galaxy M82 which is interacting with its spiral neighbour M81) and/or mergers of galaxies (e.g. the merging pair the "Antennae" NGC 4038/4039) on the other hand.

With the possible exception of the Large Magellanic Cloud, M82 is the nearest galaxy hosting multiple populations of such massive stellar clusters, thus making it a strikingly interesting object. Based on *HST* (O'Connell et al. 1995) and ground-based imaging (Satyapal et al. 1997), a swarm of young stellar clusters have been unveiled in the central regions of M82. The galactic centre is not the only region where prolific star formation has recently taken place, however. A region extending $\sim$ 400 - 1000 pc along the major axis northeast of the galactic centre, labelled M82 B (nomenclature from O'Connell & Mangano 1978), has long been suspected to have also gone through a major star formation episode several hundred million years ago. De Grijs et al. (2001) obtained *HST* multi-passband optical/near infrared observations of this fossil starburst site in which they discovered some 100 star clusters.

In this paper, we perform a detailed study of this cluster system, highlighting its cluster formation history and its chemical evolution. The paper is organized as follows. Section 2 briefly describes the irregular galaxy M82 and the fossil starburst site M82 B. Section 3 explains how we use spectral synthesis models to determine simultaneously the age and the metallicity of the M82 B clusters. Section 4 presents the cluster formation history and the chemical evolution of the M82 B region as well as evidence for the dynamical destruction over time of the clusters. Finally, our conclusions are presented in Sect. 5.

2 THE IRREGULAR GALAXY M82

M82 is the prototype starburst galaxy, being the nearest and, therefore, the best studied example of this class of galaxies. Freedman et al. (1994) estimated its distance to be 3.6 Mpc (i.e. its distance modulus is $m - M = 27.8$). Such a proximity makes it uniquely valuable for a wide range of studies regarding extragalactic star clusters. M82 belongs to the nearest group of interacting galaxies, whose other prominent members are the large spiral M81 and a fainter elliptical companion, NGC 3077. From optical images only, this set of three galaxies appears quiescent, showing little sign of tidal interactions. However, a completely different conclusion is reached from radio surveys. A map of neutral hydrogen obtained with the *Very Large Array* (Yun et al. 1994) reveals huge streams of neutral hydrogen gas connecting the three galaxies as well as several fainter ones. These HI streams are dominated by filamentary structures, loops and twists thus suggesting that the three largest members of the M81 group have gone through several close encounters. The corresponding tidal interactions have most probably triggered the formation of some of the M82 star clusters. For instance, they may be responsible for channeling large amounts of gas into the central regions of the galaxy, thus inducing the active starburst in the central regions (Rieke et al. 1993). The study of the off-centre region M82 B is particularly valuable since it has been shown to contain a more evolved star cluster system, and to have the characteristics of an older burst of star formation (e.g., O'Connell & Mangano 1978, Marcum & O'Connell 1996, de Grijs et al. 2001). Therefore, the study of M82 B will enable us to probe the galaxy's history to earlier times.

Starburst regions are often obscured so heavily by dust that their study at infrared wavelengths represents a definitive advantage with respect to the optical. De Grijs et al. (2001) used the *Wide Field Planetary Camera 2* (*WFPC2*) as well as the *Near-Infrared Camera and Multi-Object Spectrometer* (*NICMOS*), on board *HST*, to obtain high resolution imaging of M82 B in both the optical and the near infrared. Two adjacent 35" square fields, named "B1" and "B2", were imaged, the "B2" region being the closest to the galactic centre and the active starburst. Despite the fact that B1 and B2 simply correspond to two adjacent fields, this differentiation, i.e. M82 B1 and M82 B2 instead of M82 B, will often be used throughout this paper as both regions show distinct differences in their chemical evolution (see Sect. 4.4). Their *HST* observing run provided de Grijs et al. (2001) with the B, V, I and J magnitudes of the star clusters detected in M82 B. The availability of these four magnitudes allows us to disentangle the extinction, age and metallicity effects. While the way of estimating simultaneously the age and the metallicity is presented in Sect. 3.1, we now briefly summarize how de Grijs et al.(2001) derived the intrinsic colour indices of the M82 B clusters, these colour indices being used in our study.

In a $(B-V)$ vs $(V-I)$ diagram, the aging trajectories (i.e. the colour evolution with time at a given metallicity) and the extinction vector are not entirely degenerate for this choice of optical colors, showing that the BVI diagram could be used to estimate the colour excesses by which a cluster is reddened (de Grijs et al. 2001, their Fig. 12). This method also allows to derive extinction values for each cluster individually. This is useful in a galaxy like M82, which has a significant and highly variable extinction and which cannot be characterized by a single mean value for the internal extinction and reddening. Assuming that the metallicity of the M82 B clusters is roughly solar, de Grijs et al. (2001) used this property to estimate their intrinsic colour indices, their extinction and their absolute magnitudes.

Using the colour indices dereddened as explained above, de Grijs et al. (2001) determined the age distribution of the M82 B clusters, which contains information about the cluster formation rate. The age of the M82 B clusters ranges from 200 Myr to over 10 Gyr, a time interval over which clusters have been forming continuously, although not at a constant rate. The most striking feature is a strong peak of cluster formation starting about 1 Gyr ago and lasting about 600 Myr (de Grijs et al. 2001), a time roughly corresponding to the last perigalactic passage of M81 and M82 (Brouillet et al. 1991). The close match between both of these independently determined time-scales provides, therefore, very strong evidence that interactions between galaxies lead to enhanced star *cluster* formation.

While de Grijs, Bastian & Lamers (2002) study the dynamical history of the M82 B star cluster system in great detail, we focus on its chemical evolution. In order to carry out such an analysis, we refine the results obtained by de Grijs et al. (2001), that is, we redetermine both the age and the *metallicity* of the star clusters.

3 SPECTRAL SYNTHESIS

Since the pioneering papers of Tinsley (1972) and Searle, Sargent & Bagnuolo (1973), spectral population synthesis, i.e. the modeling of the spectral energy distribution of a star cluster, has become a standard technique to study the integrated stellar populations of galaxies. Assuming that stellar clusters are single-age and single abundance groups of stars, their integrated colours reflect their age and metallicity (for a given initial mass function, IMF).

In order to perform a self-consistent comparison of our results with those obtained by de Grijs et al. (2001), we use the same spectral synthesis model, i.e. the Bruzual & Charlot (1996, hereafter BC96) model. We consider the photometric properties of Simple Stellar Populations (SSPs; i.e. single-age and single abundance groups of stars) with a Salpeter IMF from 0.1 $M_\odot$ up to 125 $M_\odot$. BC96 provides the temporal evolution of the broad-band colours of such SSPs for a wide range of metallicities. In the following, we consider the three intrinsic colour indices $(B-V)_0$, $(V-I)_0$ and $(V-J)_0$ whose observational counterparts were obtained by de Grijs et al. (2001). We show below how the addition of the $(V-J)_0$ colour index enables us to estimate both the age and the metallicity of the clusters.

3.1 Disentangling age and metallicity effects

A greater age or a higher metallicity both lead to redder colours, an effect known as the age-metallicity degeneracy. For instance, in a $(B-V)_0$ versus $(V-I)_0$ plot, the iso-metallicity tracks (i.e. the locus of an SSP at different

ages for a given metallicity) and the isochrones are parallel and located in the same part of the optical colour-colour diagram, precluding therefore any simultaneous estimate of age and metallicity. De Grijs et al. (2001) also obtained the *J*-band magnitude for each cluster. Figure 1 explores the suitability of a VIJ colour-colour diagram to lift this age-metallicity degeneracy. Thin lines represent isometallicity tracks, i.e. aging trajectories, and thick lines refer to isochrones (from left to right, $\log t/\mathrm{yr} = 8.5$, 9.0, 9.5 and 10.0). The grid defined by the isometallicity tracks and the isochrones shows that a $(V-J)_0$ vs $(V-I)_0$ diagram is well suited to disentangle the effects of age and metallicity.

As mentioned in Sect. 2, the cluster intrinsic colours were determined by de Grijs et al. (2001) based on the hypothesis that the metallicity of the clusters in M82 B was roughly solar. However, the next section shows that M82 B hosts very metal-poor ($\mathrm{Z} \simeq 0.02\mathrm{Z}_\odot$) and super-solar abundance ($\mathrm{Z} > \mathrm{Z}_\odot$) clusters in addition to solar abundance ones. Therefore, one can question the validity of the present analysis which makes use of the intrinsic colours determined by de Grijs et al. (2001). The solar metallicity track and the extinction trajectories being not entirely degenerate in a $(B-V)_0$ vs $(V-I)_0$ diagram, de Grijs et al. (2001) were able to estimate the visual extinction and the colour excess for each cluster (see Sect. 2). Furthermore, the iso-metallicity tracks are at the same locus of the diagram, with the distance between two subsequent tracks of distinct metallicity being smaller than the photometric uncertainties. As a consequence, the visual extinction values and the colour excesses (or, equivalently, the intrinsic colours) estimated by de Grijs et al. (2001) on the basis of the solar metallicity hypothesis, can be used throughout this work irrespective of the metallicity of the clusters.

3.2 Accuracy of the age and metallicity estimates for unextinguished clusters

The medians of the 1σ error distributions for the different colour indices are $\sigma_{(B-V)} \simeq 0.08$, $\sigma_{(V-I)} \simeq 0.08$ and $\sigma_{(V-J)} \simeq 0.15$. Let us first assume that the uncertainties of the observed colours constitute a good approximation of the intrinsic colour uncertainties. The typical uncertainties in $(V-I)$ and $(V-J)$ are superimposed on the age-metallicity grid in Fig. 1 for the solar metallicity SSPs of 600 Myr and 10 Gyr. The corresponding uncertainties in age are the smallest for SSPs with ages from 300 Myr to 1 Gyr. For instance, for an SSP of solar metallicity the typical error in the estimated age is not greater than 40% at an age of 600 Myr, while it is as large as a factor of 2 for a 10 Gyr old SSP. This greater uncertainty at greater age, which is related to the tightening of the isochrones at $\log t/\mathrm{yr} \geq 9.5$ in the VIJ diagram, is another aspect of the decrease in sensitivity of the colour indices to ages as an SSP ages (e.g. Worthey et al. 1994). Interestingly, the diagram shows the greatest sensitivity to ages within the time interval of interest to us, namely the age of the burst of cluster formation at $\log t/\mathrm{yr} \sim 9$.

As for the accuracy of the metallicity estimates, the differences in the $(V-J)_0$ colour index between the isometallicity tracks $\mathrm{Z} = \mathrm{Z}_\odot$, $\mathrm{Z} = 0.4\mathrm{Z}_\odot$ and $\mathrm{Z} = 0.2\mathrm{Z}_\odot$ are of a similar order of magnitude as the uncertainty $\sigma_{(V-J)}$ so that we

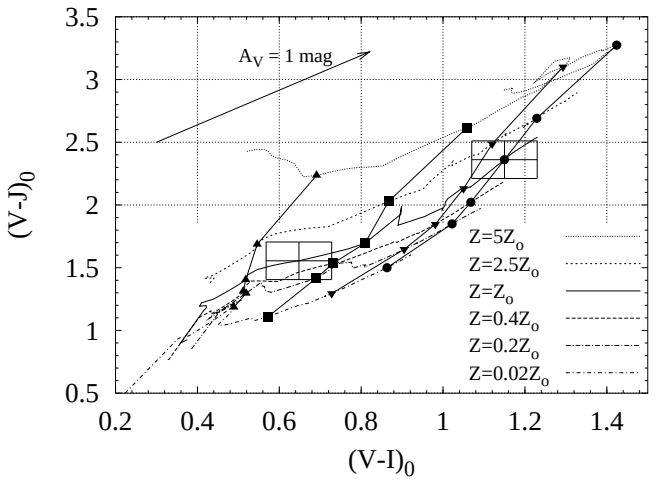

Figure 1. $(V-I)_0$ vs $(V-J)_0$ diagram of SSPs based on the BC96 model. The six thin curves represent isometallicity tracks, i.e. the locations of SSPs of different ages for six distinct metallicities. The four thick curves connecting filled symbols represent four isochrones (from left to right: triangles, $\log t/\mathrm{yr} = 8.5$; squares, $\log t/\mathrm{yr} = 9$; reversed triangles, $\log t/\mathrm{yr} = 9.5$; circles, $\log t/\mathrm{yr} = 10$). Each filled symbol is an intersection between an isochrone and an isometallicity track. The thin boxes represent the medians of the 1σ error distributions of the sample in $(V-I)$ and $(V-J)$ for two SSPs of solar metallicity at ages of 600 Myr and 10 Gyr. The arrow indicates the effects of reddening on these models, for a visual extinction $A_V = 1$ mag.

cannot easily distinguish among such close-to-solar metallicities based on the available data set. However, the VIJ colour-colour diagram can, in fact, be used to distinguish solar metallicity SSCs from very metal-poor (i.e. $\mathrm{Z} = 0.02\mathrm{Z}_\odot$) and super-solar abundance (i.e. $\mathrm{Z} > \mathrm{Z}_\odot$) populations.

We caution however that this reasoning does not take into account the *extinction* uncertainties. Figure 1 displays the extinction vector in the VIJ diagram and clearly shows that extinction uncertainties cannot be neglected as they will combine with the colour uncertainties quoted above to enlarge the error boxes in Fig. 1. This reasoning therefore applies only to clusters whose intrinsic and observed colours are not significantly different. In Sect. 4.2, we will estimate in a more careful way how the magnitude uncertainties (i.e. σ_B, σ_V, σ_I, σ_J) propagate as extinction, age, mass and metallicity uncertainties.

4 THE CLUSTER FORMATION HISTORY OF M82 B

In this section, we estimate the age, the metallicity and the mass-to-light ratio of the M82 B clusters by comparing their extinction-corrected colours to those predicted as a function of age and metallicity by BC96. We will then derive the cluster formation history of the M82 B region.

4.1 Age, metallicity and mass estimates

The age (t_{cl}) and the metallicity (Z_{cl}) of each stellar cluster are estimated simultaneously by means of a least-squares

minimisation:

$$\min\left\{S^2(t,Z)=\sum_{i=1}^{3}\left(\frac{{\rm CI}_i{}^{\rm intr}-{\rm CI}_i{}^{\rm SSP}(t,Z)}{\sigma_{{\rm CI}_i}}\right)^2\right\} \quad (1)$$

$$\Rightarrow \quad {\rm t_{cl}} \text{ and } {\rm Z_{cl}} \ .$$

In this relation, ${\rm CI}^{\rm intr}_{i=1,2,3}$ denote the three intrinsic colour indices (i.e. $(B-V)_0$, $(V-I)_0$, $(V-J)_0$) and ${\rm CI}^{\rm SSP}_{i=1,2,3}(t,Z)$ represent the corresponding BC96 integrated colours of an SSP with age t and metallicity Z. $\sigma_{{\rm CI}_{i=1,2,3}}$ are the 1σ uncertainties in the colour indices. The resulting age and metallicity distributions are shown in Figs. 2 and 3, respectively. They will be discussed, along with the other results, in the next sections. The different panels of Fig. 4 display the comparison between the BC96 colour indices for the derived ages and metallicities and the corresponding intrinsic colour indices obtained from the multicolour *HST* photometry. The 1σ error bars and, when relevant, the upper/lower limits (indicated by the arrows) of the observed colours are included. The good agreement between the observed colour indices and those derived from the BC96 spectral synthesis models illustrates the reliability of our age and metallicity estimates.

Using these age and metallicity estimates, we can now apply the age and metallicity dependent mass-to-light ratio $\frac{M}{L_V}(t,Z)$ predicted by BC96 for a single burst stellar population to derive masses m for our cluster sample.

As quoted above (Sect. 3), the mass-to-light ratio predicted by the BC96 model we use assumes a Salpeter IMF. However, there is now ample evidence that a single power-law Salpeter IMF can be ruled out at masses lower than $1\,{\rm M}_\odot$, the IMF slope becoming clearly much shallower than the Salpeter IMF. For instance, the IMF observed in the solar neighbourhood may be roughly flat at the lower end of the stellar mass spectrum or may even peak at a mass around $0.25\,{\rm M}_\odot$ and decline into the brown dwarf regime (Larson 1998). The Salpeter IMF obviously overestimates the relative number of subsolar-mass stars. These stars being those with the largest mass-to-light ratio, a Salpeter IMF causes an overestimate of the individual cluster masses, *although the relative mass distribution of our entire cluster sample remains unaffected*. If we had used more modern IMFs (e.g. Kroupa, Tout & Gilmore 1993) this would have resulted in lower cluster mass estimates, by a factor $\simeq$ 2-3 (see de Grijs et al. 2002) with respect to the mass estimates presented in this paper.

Our best age, mass and metallicity estimates for each cluster, along with their uncertainties (see the following section) are listed in Tables 1 and 2 for B1 and B2, respectively. The results are presented in Figs. 2 to 9. In these figures, the few clusters for which either B, V or I is an upper or lower limit only are represented by open symbols or dashed histograms.

4.2 Uncertainty estimates

We now address the issue of estimating the errors by which the derived cluster properties are affected. Since the extinction was derived from the BVI diagram, it is clear that uncertainties in the optical filters will propagate as extinction uncertainties. In the BVI colour-colour diagram, the extinction is the distance, measured along the reddening trajectory, from the observed point ($(B-V)$,$(V-I)$) down to the aging trajectories (Fig. 12 of de Grijs et al. 2001). Considering stellar populations older than 100 Myr, the age range of the vast majority of the clusters of our sample, the aging trajectories display the same linear growth of $(V-I)_0$ vs $(B-V)_0$, whatever the metallicity. It is therefore reasonable to approximate all the iso-metallicity tracks by the same straight line with slope and ordinate origin $m_{\rm SSP}$ ($\simeq 0.87$) and $p_{\rm SSP}$ ($\simeq 0.28$), respectively:

$$(V-I)_0 \simeq m_{\rm SSP}(B-V)_0 + p_{\rm SSP} \ . \quad (2)$$

Under this assumption, it is easy to show that the extinction modulus obeys:

$$A_V \simeq \frac{\sqrt{1+m_{\rm ext}^2}}{\sqrt{E(B-V)^2+E(V-I)^2}} \times \frac{(V-I)-m_{\rm SSP}(B-V)-p_{\rm SSP}}{m_{\rm ext}-m_{\rm SSP}} \ . \quad (3)$$

In this equation, $E(B-V)$=0.32 and $E(V-I)$=0.52 are the optical colour excesses corresponding to an extinction of one magnitude, $m_{\rm ext}$ is the slope of the reddening trajectory, i.e. $m_{\rm ext}=0.52/0.32$ (Cardelli, Clayton & Mathis 1989). Substituting these numerical values into Eq. (3), we get an estimate of the extinction dimming a cluster whose measured optical magnitudes are B, V and I:

$$A_V \simeq 4.14\,[(1+m_{\rm SSP})V - m_{\rm SSP}B - I - p_{\rm SSP}] \ . \quad (4)$$

If we assume that the BVI measurements are entirely independent, the 1σ error by which the extinction is affected derives from Eq. (4):

$$\sigma_{A_V} \simeq 4.14\sqrt{m_{\rm SSP}^2\sigma_B^2+(1+m_{\rm SSP})^2\sigma_V^2+\sigma_I^2} \ . \quad (5)$$

For each cluster, Tables 1 and 2 also list the best, minimal and maximal values of the extinction A_v. The observed points of a few clusters fall below the aging trajectories in the BVI diagram but remain nevertheless consistent with the theoretical tracks within the photometric uncertainties (de Grijs et al. 2001, their Fig. 12). In such cases, we have assumed zero extinction.

Figure 1 displays the reddening vector corresponding to an extinction of one magnitude in the VIJ diagram, i.e. the diagram used to disentangle the age and the metallicity. Since this vector is roughly parallel to the iso-metallicity tracks, the extinction uncertainties (Eq. (5)) will significantly propagate as age uncertainties. An overestimate of the extinction leads to an underestimate of the cluster age, and vice versa. In addition, the age dependent mass-to-light ratio causes the age uncertainties to propagate as mass uncertainties.

In order to perform a consistent estimate of the age uncertainties, we propagate the photometric uncertainties in each filter B, V, I and J. The age t of a cluster is a function of its $BVIJ$ photometry, that is, $(\log t) = \log t(B,V,I,J)$. Assuming that B,V,I and J are independent measurements,

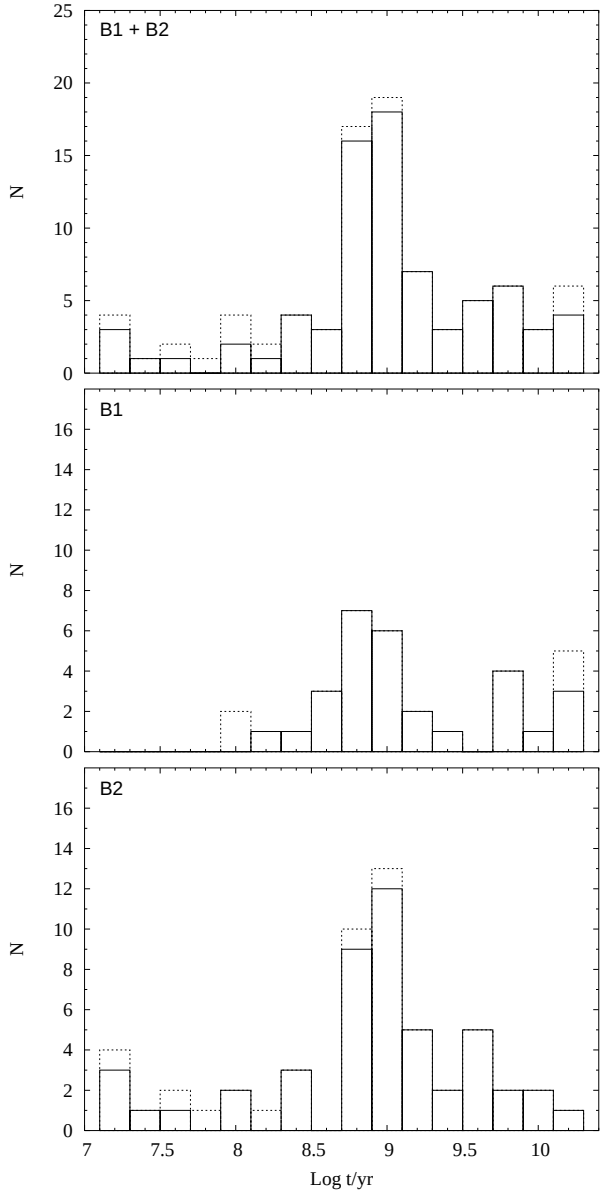

Figure 2. Age distribution of the star clusters in the entire M82 B region (top panel), in the eastern half B1 (middle panel) and the western half B2 (bottom panel). Cluster age t is expressed in years and dashed boxes represent clusters whose B, V or I is either an upper or lower limit

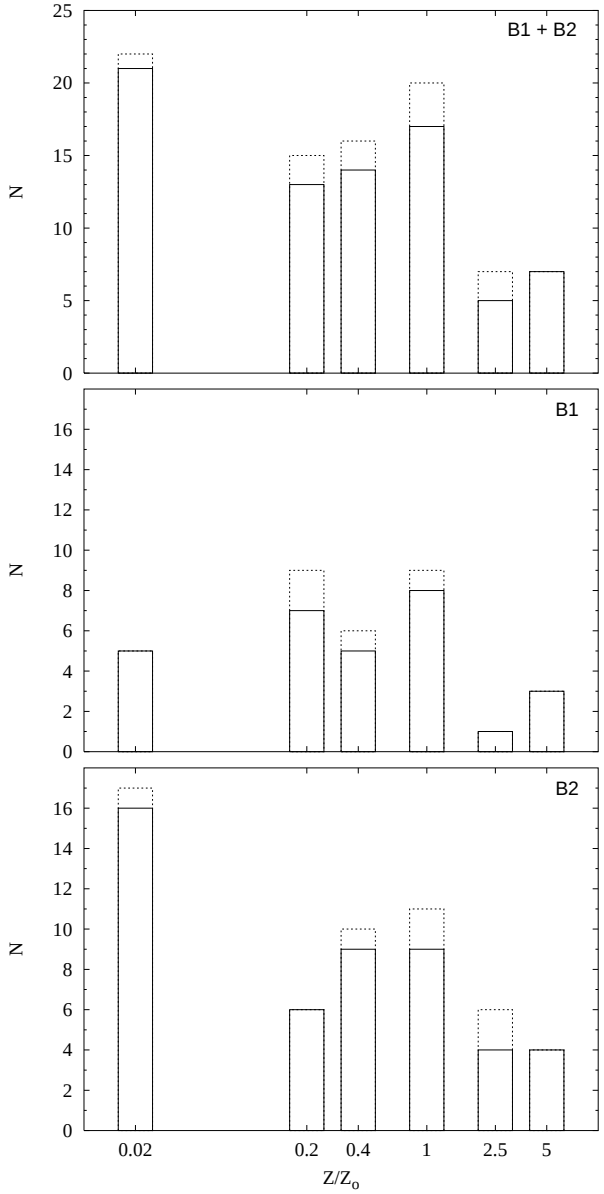

Figure 3. Metallicity distribution of the star clusters in the entire M82 B region (top panel), in the eastern half B1 (middle panel) and the western half B2 (bottom panel). Dashed boxes represent clusters whose B, V or I is either an upper or lower limit

$\sigma_{\log t}$, the 1σ error in $\log t$ we aim to estimate, is given by:

$$\sigma^2_{\log t} = \sigma^2_B \left(\frac{\partial(\log t)}{\partial B}\right)^2_{V,I,J} + \sigma^2_V \left(\frac{\partial(\log t)}{\partial V}\right)^2_{B,I,J} + \sigma^2_I \left(\frac{\partial(\log t)}{\partial I}\right)^2_{B,V,J} + \sigma^2_J \left(\frac{\partial(\log t)}{\partial J}\right)^2_{B,V,I} . \quad (6)$$

In this equation, σ_B is the B magnitude uncertainty, etc, $(\partial(\log t)/\partial B)_{V,I,J}$ is the partial derivative of the age logarithm with respect to B while keeping V,I,J constant, etc.

Equation (6) can be rewritten as:

$$\sigma^2_{\log t} = [\delta_B(\log t)]^2 + [\delta_V(\log t)]^2 + [\delta_I(\log t)]^2 + [\delta_J(\log t)]^2 \quad (7)$$

where $\delta_B(\log t)$ is the variation in $\log t$ caused by a 1σ change in the B magnitude while keeping the V, I, J ones to their best values, etc. The different terms of the right-hand side of Eq. (7) can therefore be derived by computing the cluster age for each of the following combinations of observed magnitudes: $(\log t)(B,V,I,J)$, $(\log t)(B \pm \sigma_B,V,I,J)$, $(\log t)(B,V \pm \sigma_V,I,J)$, $(\log t)(B,V,I \pm \sigma_I,J)$, $(\log t)(B,V,I,J \pm \sigma_J)$, B, V, I and J being the best magnitude values. Figure 5 shows how such 1σ individual changes

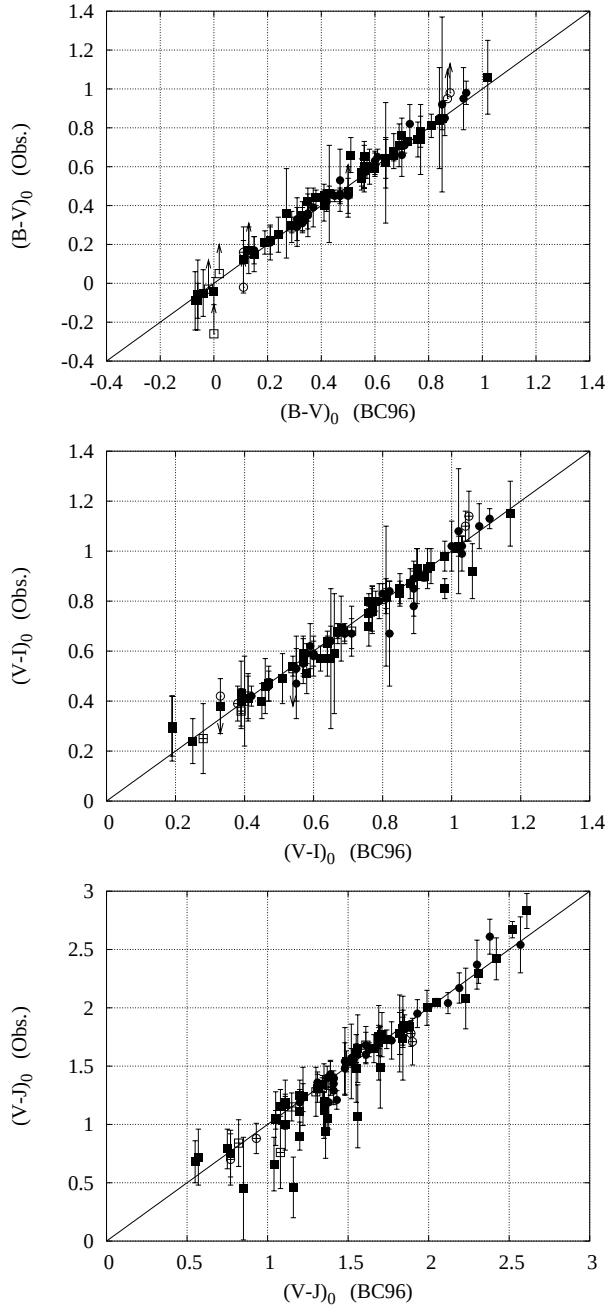

Figure 4. Comparison between the intrinsic (i.e. observed and dereddened) colour indices and those of the BC96 model at the metallicities and ages determined for the B1/B2 clusters (circles/squares). The 1σ error bars are also indicated. When either B, V or I is an upper or lower limit, the cluster is represented by an open symbol

in the observed magnitudes of a cluster affect its location in the VIJ diagram. The left and right panels illustrate the cases of B1-43 and B2-32, respectively. The crossed-circle indicates the location of the cluster corresponding to its best magnitude values. The diagrams illustrate that changing these values by the following amounts:

a) $+\sigma_B$ or $-\sigma_V$ or $+\sigma_I$ or $+\sigma_J$ (corresponding to the stars in the panels of Fig. 5) leads to an increase of the age estimate. Equation (4) indeed indicates that increasing B or I, or decreasing V leads to a decrease of the extinction and, therefore, to a shift towards the right part of the VIJ diagram, i.e. towards older ages. Increasing the J magnitude does not affect the extinction but leads nevertheless to an age increase through a downwards shift in the VIJ diagram;
b) a similar reasoning shows that changing the magnitudes by $-\sigma_B$ or $+\sigma_V$ or $-\sigma_I$ or $-\sigma_J$ (the diamonds in the panels of Fig. 5) with respect of their best values lowers the cluster age estimate.

Summing quadratically the age changes derived from the series (a) will therefore provide the age "upper" error bar, while summing quadratically the age changes derived from the series (b) will provide the "lower" age error bar, that is:

$$\begin{aligned}(+\sigma_{\log t})^2 = &[(\log t)(B,V,I,J) - (\log t)(B+\sigma_B,V,I,J)]^2 \\ &+ [(\log t)(B,V,I,J) - (\log t)(B,V-\sigma_V,I,J)]^2 \\ &+ [(\log t)(B,V,I,J) - (\log t)(B,V,I+\sigma_I,J)]^2 \\ &+ [(\log t)(B,V,I,J) - (\log t)(B,V,I,J+\sigma_J)]^2 \quad (8)\end{aligned}$$

and

$$\begin{aligned}(-\sigma_{\log t})^2 = &[(\log t)(B,V,I,J) - (\log t)(B-\sigma_B,V,I,J)]^2 \\ &+ [(\log t)(B,V,I,J) - (\log t)(B,V+\sigma_V,I,J)]^2 \\ &+ [(\log t)(B,V,I,J) - (\log t)(B,V,I-\sigma_I,J)]^2 \\ &+ [(\log t)(B,V,I,J) - (\log t)(B,V,I,J-\sigma_J)]^2 \quad (9)\end{aligned}$$

for the "upper" and "lower" error bars in $\log t$, respectively.

As already mentioned, the age uncertainties propagate as mass uncertainties through the age dependent mass-to-light ratio. The errors affecting the cluster mass and metallicity are derived in a way similar to those affecting the age: we individually propagate the magnitude uncertainties and we then compute the lower/upper error bars by summing quadratically the shifts leading to mass and metallicity estimates smaller/greater than the best ones. The 1σ mass error we derive thus takes into account the uncertainties affecting both the intrinsic luminosity of the cluster and its mass-to-light ratio. The luminosity uncertainties originate from

(i) the visual magnitude uncertainty (σ_V),
(ii) the extinction uncertainty, which depends on the optical magnitude uncertainties, i.e. σ_B, σ_V and σ_I (see Eq. (5)).

The mass-to-light ratio uncertainties are driven by the age and metallicity uncertainties, which both depend on the $BVIJ$ photometry. The metallicity uncertainties however mostly reflect the J magnitude 1σ error. More than two thirds of our clusters are characterized by:

$$Z_{\max} = Z(B,V,I,J-\sigma_J) \quad \text{and} \quad Z_{\min} = Z(B,V,I,J+\sigma_J)\,. \quad (10)$$

This result is not unexpected: the extinction vector being roughly parallel to the aging trajectories, the influence of the extinction uncertainties (driven by the optical uncertainties) upon the metallicity is strongly reduced.

The age, mass and metallicity estimates (minimal, best and maximal values) are listed in Tables 1 and 2 for B1 and

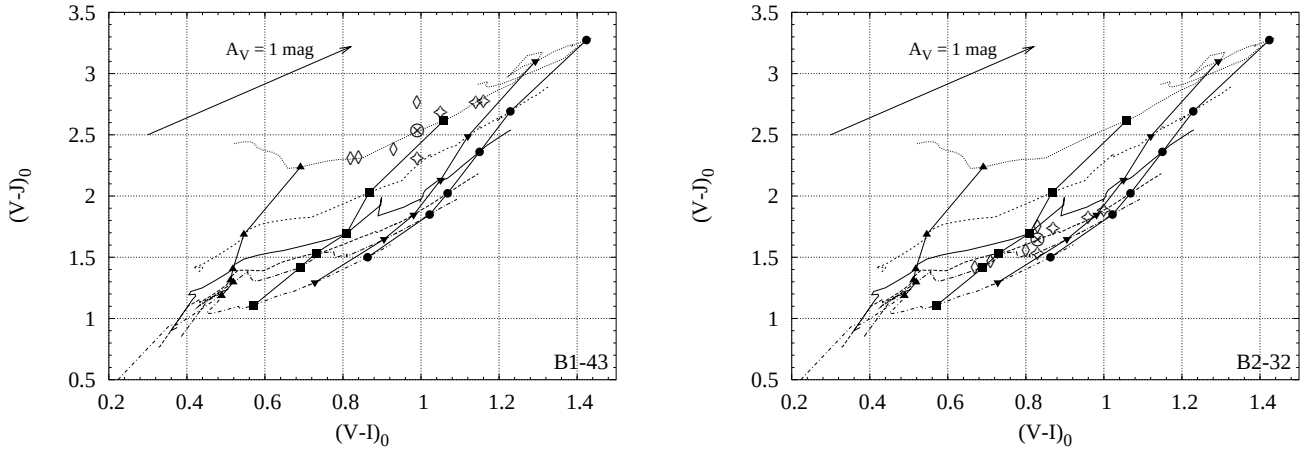

Figure 5. Impact of the individual propagation of the B, V, I and J magnitude uncertainties upon the cluster location in the VIJ diagram. The crossed circle stands for the location corresponding to the best magnitude values, the four-branch stars correspond to the best values shifted by $+\sigma_B$ or$-\sigma_V$ or $+\sigma_I$ or $+\sigma_J$, and the diamonds are the cluster locations if the best values have been shifted by $-\sigma_B$ or$+\sigma_V$ or $-\sigma_I$ or $-\sigma_J$. Left panel: B1-43; right panel: B2-32

B2, respectively. Our photometric mass estimates show an accuracy of well within an order of magnitude. Tables 1 and 2 show that the mass estimates are more robust than the age estimates (see also Fig. 8). This pattern comes from the combination of two effects. Firstly, the mass-to-light ratio grows with time at a slower rate than time itself (i.e. the evolution of $\log(m/L_v)$ vs $\log t$ exhibit a linear behaviour with a slope of less than unity, see BC96). In addition, the impact upon the mass estimate of mass-to-light ratio variations is partially counterbalanced by extinction variations. In order to illustrate this, let us consider a cluster for which the extinction has been overestimated. The adjustment of the extinction to a more appropriate (i.e. lower) value leads to a smaller cluster intrinsic brightness which, alone, would lower the photometric mass estimate. At the same time however, the extinction decrease causes a rise of the cluster age estimate (see the extinction vector in Fig. 5) and, therefore, an increase of the cluster mass-to-light ratio. These effects, a luminosity decrease and a mass-to-light ratio increase, act upon the mass estimate in opposite ways. For instance, considering a roughly solar metallicity model, a decrease of 0.6 magnitude in A_V causes an age increase of $\log t \simeq 0.5$ at the time of the burst (see Fig. 5). Accordingly, the mass-to-light ratio grows by a factor of $\simeq 2.7$. The new mass estimate is thus larger than the previous one by a factor $2.7/2.5^{0.6} \simeq 1.6$. In summary, while an age increase leads to a growth of the mass estimate through the age dependent mass-to-light ratio, this mass increase is reduced by a decrease in extinction, which acts in the opposite way. It is worth to mention that this extinction-induced reduction of the mass variation is not so important for intermediate and old populations. In fact, due to the tightening of the isochrones at older age (see Fig. 5), a given extinction variation corresponds to a greater age range at older age than at the burst epoch and, therefore, to a larger mass-to-light ratio variation. The relative reduction of the mass uncertainty thanks to the extinction variation is thus much weaker at old age than at the burst age.

As a result of the variations with time of the mass-to-light ratio, the lower and upper mass limits are strongly coupled to the lower and upper age limits, respectively.

4.3 The cluster formation history

Figure 2 shows the age distributions of the clusters in the entire M82 B region (top panel), in regions B1 (middle panel) and B2 (bottom panel). Clusters have been forming continuously, their age ranging from more than 10 Gyr down to about 10 Myr. In addition, the B1 and B2 regions exhibit a period of enhanced cluster formation, from about 1.5 Gyr ago until 500 Myr ago. We therefore confirm the main result of de Grijs et al. (2001), although our peak of cluster formation is slightly older, $\sim$ 1 Gyr (see also de Grijs et al. 2002, for more details). The M82 B burst was followed by a sharp decline in the cluster formation rate. Less than one fifth of the clusters are younger than 500 Myr. Starbursts are likely to be strongly self-limited by supernova-driven outflows which remove the remaining cool gas from the immediate starburst region. It is interesting to note that the B2 region, which is closer to the active starburst, has formed a few clusters more recently than B1.

It has long been suspected that the tidal interactions between the M81 group members (i.e. M81, M82 and NGC 3077) are responsible for the starburst nature of M82 and for the HI bridges connecting these galaxies. Brouillet et al. (1991) used an N-body model, representing M81, M82 and NGC 3077, to simulate the deformations of the neutral hydrogen distribution due to the tidal interactions: their results reproduce the observed HI bridges and tails rather well. According to their simulation, the last perigalactic passage of M82 and M81 took place some 500 Myr ago. The onset of the burst about 1.5 Gyr ago is thought, therefore, to coincide with the beginning of the tidal interactions between M82 and its prominent neighbour M81.

Table 1. Derived properties of the cluster sample in M82 B1, from left to right the age, the mass, the metallicity and the extinction

ID	$\log t/\mathrm{yr}$			$\log m/\mathrm{M}_\odot$			$\mathrm{Z}/\mathrm{Z}_\odot$			A_V		
1...	8.92	9.80	10.18	5.03	5.58	5.88	0.20	0.40	1.00	0.92	1.30	1.38
4...	7.81	8.41	8.89	4.98	5.24	5.43	1.00	1.00	2.50	2.00	2.48	2.69
5...	9.98	10.18	10.18	5.86	6.01	6.01	0.20	0.20	0.40	0.42	0.73	1.04
6...	7.91	8.21	8.83	5.26	5.34	5.57	0.02	1.00	1.00	1.47	1.86	1.97
7...	9.03	9.20	9.37	5.57	5.68	5.78	0.20	0.40	0.40	0.22	0.51	0.80
8...	8.69	8.86	8.98	5.24	5.29	5.36	0.02	0.02	0.20	0.12	0.35	0.58
9...	8.33	8.71	8.82	4.20	4.30	4.43	5.00	5.00	5.00	0.00	0.00	0.73
11...	8.89	9.01	9.17	5.35	5.40	5.49	0.02	0.20	0.20	0.06	0.34	0.62
12...	8.72	9.02	9.31	4.78	4.84	5.03	0.20	1.00	2.50	0.00	0.23	0.97
14...	8.37	8.78	9.05	5.04	5.25	5.38	0.40	1.00	2.50	0.89	1.39	1.89
16...	8.60	10.18	10.18	4.87	5.76	5.76	0.02	0.20	0.40	1.71	1.71	2.88
17...	8.37	8.81	9.16	4.50	4.63	4.73	5.00	5.00	5.00	0.01	0.67	1.33
18...	8.85	8.98	9.05	5.51	5.56	5.60	0.20	0.20	0.40	0.40	0.59	0.78
20...	9.50	9.83	10.18	5.85	6.00	6.19	0.02	0.02	0.02	0.09	0.32	0.55
22...	8.37	8.71	8.83	5.15	5.30	5.36	1.00	1.00	2.50	0.70	0.98	1.26
24...	8.68	8.90	9.06	5.13	5.20	5.32	0.20	0.20	0.40	0.20	0.57	0.94
25...	9.30	9.80	10.18	5.28	5.54	5.82	0.02	0.02	0.02	0.48	0.80	1.12
26...	8.22	8.66	8.77	4.14	4.33	4.38	0.20	1.00	2.50	0.00	0.00	0.23
28...	8.96	9.00	9.08	5.95	5.98	6.01	0.20	0.20	0.20	0.46	0.55	0.64
29...	7.82	8.75	8.98	4.20	4.72	4.75	0.02	0.40	1.00	0.45	1.07	1.69
30...	8.98	9.20	9.36	5.03	5.13	5.20	0.02	0.02	0.20	0.08	0.29	0.50
32...	8.94	9.74	10.18	4.68	5.10	5.42	0.02	0.02	0.02	0.00	0.34	0.85
33...	7.10	10.18	10.18	3.51	5.01	5.01	0.02	0.20	0.40	0.00	0.20	2.45
36...	8.60	10.00	10.18	4.86	5.91	6.10	0.20	1.00	1.00	0.85	1.01	1.83
37...	9.13	9.38	10.07	5.70	5.82	6.26	0.20	0.20	0.40	0.63	0.86	1.09
38...	8.10	8.68	8.92	4.37	4.67	4.71	0.40	2.50	2.50	0.13	0.75	1.37
40...	7.73	8.50	8.95	3.70	3.90	4.13	0.20	1.00	2.50	0.00	0.54	1.29
41...	8.22	8.75	8.90	4.79	4.97	5.01	0.20	0.40	1.00	0.63	1.03	1.43
43...	8.62	8.90	9.28	4.31	4.44	4.59	2.50	5.00	5.00	0.00	0.48	1.03

4.4 The chemical evolution

The M82 B cluster system is characterized by a wide range of metallicities (see Fig. 3) as it hosts both very metal-poor clusters ($\mathrm{Z}\simeq 0.02\mathrm{Z}_\odot$) and super-solar abundance ones ($\mathrm{Z}>\mathrm{Z}_\odot$). Such a pattern must be related to the region's chemical evolution. In order to illustrate this, each panel of Fig. 6 shows the cluster age distribution at a given metallicity for regions B1 (left column) and B2 (right column). The metallicities shown are, from top to bottom, $Z = 0.02Z_\odot$, $0.2Z_\odot$, $0.4Z_\odot$, $1Z_\odot$, $2.5Z_\odot$, $5Z_\odot$.

From the birth of its first clusters until about 1 Gyr ago, M82 B formed clusters with roughly solar and subsolar metal abundances only. In both subregions B1 and B2, the formation of the first clusters with significantly supersolar (i.e. $Z > Z_\odot$) metallicities coincides with the onset of the burst. The stellar ejecta from the evolution of older stars have most probably contributed to the chemical enrichment. While this chemical evolution up to super solar metallicities at the burst epoch is a feature in common for B1 and B2, both subregions nevertheless exhibit a striking difference regarding the most metal-poor clusters. At the time of the burst, and despite the chemical enrichment noticed above, B2 managed to form a significant subpopulation of very metal-poor clusters (i.e. $Z \simeq 0.02Z_\odot$) with respect to B1 (top panels in Fig. 6). We stress that half of these B2 clusters have very well-constrained ages ($(\log t_{\max} - \log t_{\min}) \leq 0.5$) and metallicities ($Z_{\max} = 0.2$), so that we probably do not face a spurious effect.

Either some interstellar gas in B2 managed to escape the chemical enrichment driven by the older stellar populations, or alternatively some "fresh" metal-poor gas was injected into the B2 region shortly before the burst. Whereas the first scenario is hard to explain, the second is more appealing. A large amount of circumgalactic cold material is orbiting M82, stripped from the gas-rich outskirts of the M81 group spirals by tidal interactions. These interactions involve quite a few galaxies, of which three are of a non-negligible size (i.e. M81, M82 and NGC 3077). It is therefore not unreasonable to assume that tidal interactions and gas tidal stripping were at least somewhat important even before M81 and M82 almost collided about 0.5 Gyr ago. If the bridges of circumgalactic gas were indeed already present 1 Gyr ago (i.e. 500 Myr prior to the perigalactic passage), gas infall from this reservoir onto the B2 region may have induced the formation of this subpopulation of metal-poor clusters. Alternatively, some metal-poor gas associated with the M82 outskirts could have been driven onto B2 by tidal interactions.

In comparing the properties of the clusters of B1 with those of B2, we implicitely assume that their respective current and birth locations, with respect to the galactic centre, coincide. The validity of this assumption may be questioned as, at the distance from the centre of region B, one would expect M82's differential rotation (Shen & Lo 1995) to have

Table 2. Derived properties of the cluster sample in M82 B2, from left to right the age, the mass, the metallicity and the extinction

ID	$\log t/\mathrm{yr}$			$\log m/\mathrm{M}_\odot$			$\mathrm{Z}/\mathrm{Z}_\odot$			A_V		
1...	8.68	10.09	10.15	4.35	5.25	5.31	1.00	1.00	2.50	0.00	0.00	0.64
4...	8.79	8.91	8.98	5.41	5.45	5.46	5.00	5.00	5.00	0.49	0.73	0.96
5...	7.49	8.76	9.20	4.89	5.38	5.47	0.02	0.02	0.40	0.75	1.34	1.92
8...	8.73	9.01	9.62	5.55	5.59	6.00	0.40	1.00	2.50	2.72	3.35	3.98
12...	9.27	9.44	9.58	6.60	6.71	6.82	1.00	1.00	1.00	0.83	0.94	1.06
13...	9.36	9.98	10.18	5.38	5.77	5.88	0.20	0.20	0.40	0.54	0.85	1.16
14...	8.31	9.01	9.81	4.78	5.05	5.56	5.00	5.00	5.00	1.00	1.83	2.66
15...	8.87	8.96	9.08	5.88	5.98	6.00	0.20	1.00	1.00	2.88	3.20	3.52
17...	8.93	9.60	10.18	5.27	5.62	6.04	0.20	0.20	0.40	0.62	1.18	1.74
18...	7.10	7.16	8.18	4.64	4.64	5.29	0.02	0.20	0.40	3.89	4.40	4.70
21...	7.09	7.31	7.72	5.06	5.16	5.42	2.50	2.50	2.50	4.11	4.18	4.98
23...	7.21	9.01	10.18	4.25	4.75	5.77	0.02	1.00	2.50	0.00	1.70	3.24
25...	7.77	8.41	9.12	4.72	4.95	5.25	0.20	0.40	1.00	0.61	1.26	1.70
26...	8.86	9.01	9.13	5.65	5.72	5.77	0.02	0.02	0.20	0.48	0.58	0.68
28...	7.01	7.18	8.00	3.67	4.03	4.62	0.02	0.20	0.40	1.93	2.30	3.14
29...	7.18	8.01	9.74	3.53	3.81	4.54	0.02	0.20	0.40	0.29	1.06	1.95
30...	8.79	9.00	9.29	5.15	5.21	5.22	0.02	0.02	0.20	1.14	1.56	1.98
32...	8.87	9.16	9.80	5.09	5.19	5.62	0.02	0.40	1.00	1.20	1.66	2.13
33...	7.38	8.46	9.16	3.75	4.30	4.51	2.50	5.00	5.00	0.00	1.13	2.12
34...	7.20	8.31	8.83	3.57	4.09	4.22	0.02	1.00	2.50	0.76	1.29	1.52
36...	9.27	9.30	9.68	5.35	5.37	5.60	0.20	0.20	0.40	0.00	0.00	0.02
37...	7.53	7.60	7.75	5.19	5.25	5.34	0.40	2.50	2.50	2.43	2.43	3.58
38...	8.90	9.16	9.30	4.52	4.76	4.86	0.02	0.02	0.20	0.00	0.00	0.00
39...	7.84	8.81	9.02	4.02	4.42	4.56	0.20	1.00	2.50	0.00	0.00	0.80
40...	8.69	8.81	8.90	5.23	5.27	5.31	0.02	0.02	0.02	0.42	0.54	0.66
41...	8.77	8.86	8.98	5.89	5.91	5.96	2.50	2.50	2.50	0.54	0.74	0.92
43...	9.06	9.06	9.35	4.54	4.54	4.84	0.02	0.02	0.02	0.00	0.00	0.00
45...	8.77	9.65	10.18	4.94	5.44	5.81	0.02	0.02	0.02	1.25	1.54	2.33
47...	9.50	10.18	10.18	4.64	5.00	5.00	0.02	0.02	0.02	0.00	0.00	0.45
48...	8.33	8.81	9.05	4.23	4.46	4.52	0.02	0.02	1.00	0.56	1.04	1.18
49...	9.09	9.51	10.18	5.49	5.71	6.28	0.20	0.40	1.00	0.23	0.63	1.02
50...	7.17	7.20	8.81	4.06	4.09	4.82	0.02	0.40	0.40	1.39	2.12	2.50
52...	9.50	9.70	9.85	4.89	5.07	5.16	0.02	0.02	0.02	0.00	0.00	0.07
54...	8.15	8.96	9.08	4.21	4.55	4.57	0.02	0.02	0.40	0.00	0.01	0.54
55...	8.60	8.71	9.07	3.93	3.98	4.07	0.02	1.00	2.50	0.00	0.00	0.00
56...	8.71	9.11	9.16	4.84	4.91	4.97	1.00	1.00	2.50	0.00	0.11	0.83
57...	8.46	8.76	9.05	5.15	5.28	5.38	2.50	5.00	5.00	0.63	1.13	1.63
59...	6.70	8.06	9.72	3.99	4.65	5.34	0.02	0.40	1.00	1.93	2.88	3.81
60...	7.96	9.01	9.70	4.14	4.60	4.91	0.02	0.02	0.20	0.23	0.77	1.33
62...	8.98	9.65	9.78	4.08	4.47	4.57	0.02	0.02	0.20	0.00	0.00	0.38
63...	8.70	8.96	9.10	4.66	4.83	4.83	0.02	0.02	0.40	0.49	0.75	0.99
64...	9.40	9.68	10.18	4.40	4.58	4.98	0.02	0.20	0.40	0.00	0.00	0.34
65...	9.14	9.72	10.17	5.16	5.51	5.72	0.02	0.02	0.02	0.52	0.84	1.16
66...	8.20	8.76	8.99	3.80	3.95	3.99	0.40	2.50	2.50	0.00	0.16	1.06
67...	8.76	8.91	9.01	5.21	5.23	5.28	0.20	0.40	1.00	1.21	1.45	1.67
68...	8.73	9.23	9.59	4.52	4.69	4.96	0.02	0.40	1.00	0.00	0.39	0.90
69...	8.72	9.06	9.81	4.01	4.16	4.60	0.02	0.40	2.50	0.00	0.00	0.00
70...	8.99	9.16	9.33	4.95	5.12	5.19	0.02	0.02	0.02	0.05	0.17	0.29

caused the starburst area to disperse. However, the lack of bright clusters like those in M82 B outside this region does not meet this expectation and, on the contrary, indicates that the fossil starburst region has remained relatively well constrained. The reason for this is likely found in the complex structure of the disc. It is well-known that the inner ~ 1 kpc of M82 (i.e. the radial extent of M82 B) is dominated by a stellar bar (e.g., Wills et al. 2000) in solid-body rotation. From observations in other galaxies, it appears to be a common feature that central bars are often surrounded by a ring-like structure. If this is also true for M82, it is reasonable to assume that stars in the ring are trapped, and therefore cannot move very much in radius because of dynamical resonance effects. As a consequence, not only has the fossil starburst site managed to stay together, both subregions B1 and B2 may also have conserved their own specificity for about 1 Gyr (see also de Grijs 2001). In the next section, we show that the presence (B2), or the absence (B1), of a subpopulation of very metal-poor clusters at the burst epoch is not the only difference between B1 and B2.

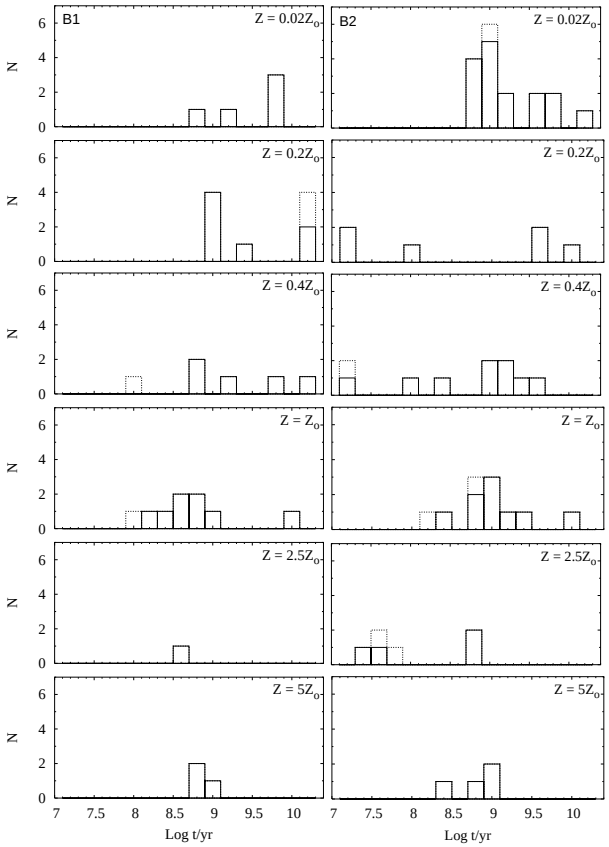

Figure 6. Age distributions of the M82 B clusters at a given metallicity, from $Z = 0.02Z_\odot$ (top) to $Z = 5Z_\odot$ (bottom). Left/right column: B1/B2 sample. Dashed boxes represent clusters whose B, V or I is either an upper or lower limit

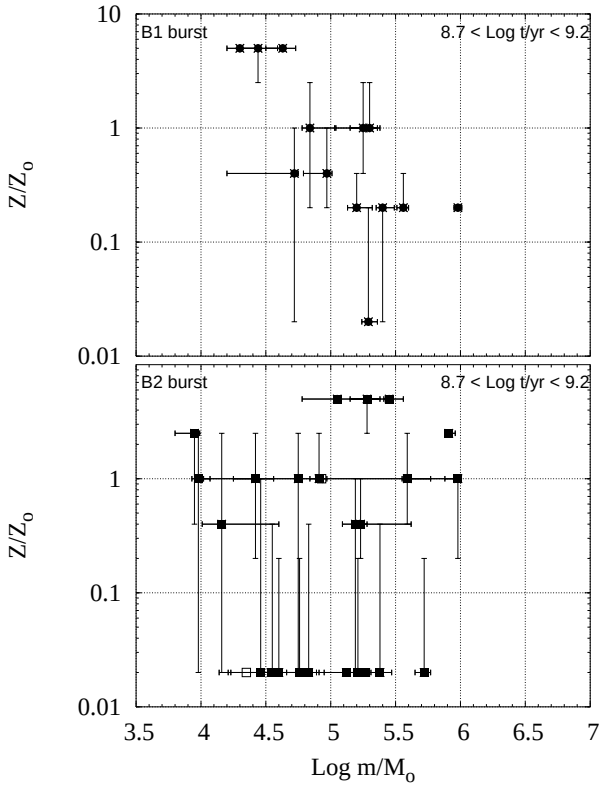

Figure 7. Mass-metallicity diagrams for the clusters formed during the burst of cluster formation ($0.5 < t < 1.5$ Gyr). The cluster mass m is expressed in units of $M_\odot$. Top/bottom panel: B1/B2. Open symbols refer to clusters of which one of the observed magnitudes B, V or I is ill-determined (upper or lower limit)

4.4.1 Did the B1 clusters go through a self-enrichment phase?

A high-pressure medium favours the formation of pressure-bound clouds, which may be the progenitors of future stellar clusters. For instance, Fall & Rees (1985) suggested that the formation of the halo GCs in our Galaxy occured in dense and cold clouds which are in pressure equilibrium with a hot and diffuse background. This two-phase medium is thought to have been formed by the collapse of the protoGalaxy. In the frame of their theory, the GC progenitor clouds are thermally supported and made of primordial gas. To explain the metallicities of the Galactic halo GCs, Parmentier et al. (1999) further developed this picture for GC formation and proposed that the halo GC gaseous progenitors went through a self-enrichment phase. A self-enrichment scenario assumes the formation of a first generation of stars in the central regions of each proto-globular cluster cloud. When the massive stars explode as Type II supernovae, they chemically enrich the surrounding cloud gas and trigger the formation of a second stellar generation, more metal-rich than the first one. These second generation stars form the proto-globular cluster. Supernovae having long been thought to disrupt the cloud of gas out of which they have formed, Parmentier et al. (1999) studied the ability of pressure-truncated clouds to retain supernova ejecta and further showed that such a process is able to explain Galactic halo GC metallicities. Assuming that the number of supernovae is the maximum number predicted by their model (i.e. a few hundred), a self-enrichment episode in pressure-bound clouds shows up as a correlation between the mass and the achieved metallicity of the progenitor cloud in the sense that the least massive clouds are the most metal-rich. Such a trend emerges because if the bound pressure is higher, the mass of the pressure-truncated cloud will be lower, and its ability to retain supernova ejecta will be greater. Regarding the resulting system of GCs, a tight mass-metallicity correlation should not be expected, however. The star formation efficiency (i.e. the ratio between the mass of the second stellar generation and the mass of gas) and the number of supernovae (which determines the amount of metals dispersed within the cloud) may vary from cloud to cloud, imprinting therefore a scatter on the initial mass-metallicity correlation (see Parmentier & Gilmore 2001 for a more detailed discussion). In spite of this scatter, Parmentier & Gilmore (2001) showed that such a mass-metallicity correlation is statistically present in the Milky Way Old Halo, i.e. the group of old and coeval halo GCs (e.g. Rosenberg et al. 1999). At this stage, it is worth keeping in mind that the search for a mass-metallicity relation must be restricted to a coeval population of clusters. The (surviving) correlation primarily reflects the

variations in the pressure by which the clouds are bound and has nothing to do with the chemical enrichment with time.

Both the M82 interstellar medium and the hot protogalactic background are high-pressure mediums. Therefore, a tempting question is whether the almost coeval population of clusters formed during the burst ($0.5 < t < 1.5\,\mathrm{Gyr}$) have undergone a self-enrichment process in pressure-truncated progenitor clouds. These M82 B clouds were most likely mainly supported by non-thermal effects (e.g. turbulence and magnetic fields) and resembled more closely giant molecular clouds than the neutral hydrogen clouds described by the Fall & Rees (1985) theory. As mentioned above, however, the key parameter leading to a trend between the mass and the metallicity of stellar clusters is the pressure of the medium in which their progenitor clouds were embedded. It is widely believed that the boundary of giant molecular clouds is set by pressure balance with the surrounding, more diffuse, interstellar medium (e.g. McLaughlin & Pudritz 1996). Therefore, the hypothesis of a mass-metallicity relation among the clusters of the M82 B system makes sense. In order to explore the possibility of a self-enrichment event (superimposed on an unavoidable pre-enrichment phase owing to the young age of the clusters), we now search for such a mass-metallicity correlation among the $\simeq$1 Gyr old clusters in the B1 and B2 regions. Again, B1 and B2 exhibit different patterns (see Fig. 7, B1/B2: top/bottom panel). The B1 sample shows a mass-metallicity correlation in the sense expected by the self-enrichment model, i.e. the most metal-rich clusters are, on average, least massive: the linear Pearson correlation coefficient is $r = -0.70$, corresponding to a correlation probability of $\wp = 99.5\%$. The scatter in metallicity at a given mass interval (e.g. $10^5 < m < 3 \times 10^5 M_\odot$) remains significant but this is not unexpected because of the scatter sources mentioned above. The age of the vast majority of the B1 burst clusters is well constrained ($(\log t_{\max} - \log t_{\min}) \leq 0.7$ for 11 of the 13 clusters) and so is their mass (see the horizontal error bars in the top panel of Fig. 7). In addition, the metallicity error bars are rather limited as well. As a result, the error bars, both in mass and metallicity, do not significantly corrupt the correlation. In contrast to B1, the B2 burst clusters do not exhibit any mass-metallicity correlation. Removing the most metal-poor clusters (i.e. those assumed to have formed from circumgalactic gas) does not change the situation. This difference between the B1 and B2 mass-metallicity diagrams might be related to the formation of some metal-poor clusters in B2 at the burst epoch. If these low metal abundance clusters indeed formed out of the arrival of "fresh" gas, a shock wave would have accompanied the gas injection, perturbing the external pressure and preventing therefore any self-enrichment in pressure-bound clouds.

While the scenario presented above is tentative, the fact that B1 and B2 exhibit different behaviours from the points of view of the chemical evolution (top panels of Fig. 6) and of the mass-metallicity relation (Fig. 7) is puzzling and suggests actual differences between the cluster formation histories in both regions at the time of the burst.

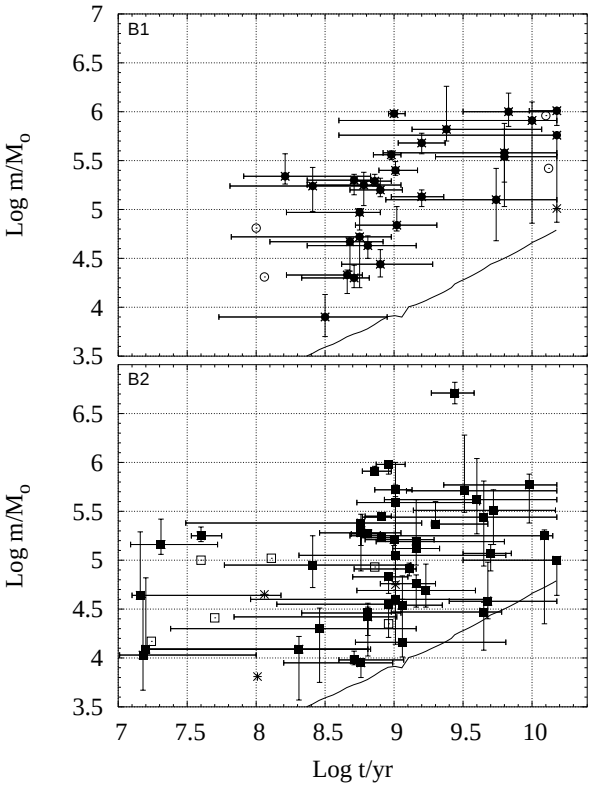

Figure 8. Evolution with time of the mass of the detected clusters. Circles and squares correspond to B1 and B2 clusters respectively. Open symbols refer to clusters whose B, V or I is either an upper or lower limit. Asterisks represent clusters with very badly constrained ages: $t_{\min} \simeq 10 - 20\,\mathrm{Myr}$ and $t_{\max} \simeq 10\,\mathrm{Gyr}$. The solid line is the selection limit imposed by the detection luminosity threshold for an SSP with Z = 0.02 Z$_\odot$

4.5 Dynamical disruption of the SSCs

Figure 8 shows the evolution with time of the mass of the clusters in B1 and B2. The most striking feature is the deficit in low-mass clusters (i.e. $\log m/M_\odot < 5.5$) during the pre-burst phase ($\log t/\mathrm{yr} \geq 9.2$) with respect to the burst period. However, this effect is likely mainly caused by an observational bias, that is, due to the fading of stellar populations with time low-mass clusters are more difficult to detect at old and intermediate age than at young ages (see also de Grijs et al. 2002).

In order to consider only cluster candidates with good photometry, de Grijs et al. (2001) selected clusters brighter than $V = 22.5$ (corresponding to the 100% completeness limit). The equivalent upper limit in absolute visual magnitude is $M_V = -5.3$. The temporal evolution of the corresponding lower mass limit is shown as the solid line in the two panels of Fig. 8. This fading line is based on the mass-to-light ratio predicted by the BC96 model for a metallicity of Z$\simeq$ 0.02 Z$_\odot$. We can afford to use a model with such a low metallicity, and therefore a low mass-to-light ratio, since very metal-poor clusters are detected at any age up to the burst epoch. A comparison of the fading line with the distribution of points in top and bottom panels of Fig. 8 shows that the deficit in

low-mass clusters at large age cannot be accounted for solely by the selection effect, especially in B1.

Systems of young clusters are well known to show a cluster initial mass function scaling as $\mathrm{d}N \propto m^{-\alpha}\mathrm{d}m$, where m is the cluster initial mass and $\mathrm{d}N$ is the number of clusters with mass between m and $m+\mathrm{d}m$. Observations show that the slope α is $\simeq 2$ (Zhang & Fall 1999; Whitmore et al. 1999; Bik et al. 2002; see also Sect. 4.6). At an intermediate age of 5 Gyr ($\log t \simeq 9.7$), the mass detection threshold is $3\times10^4\mathrm{M}_\odot$ ($\log m = 4.5$). If the cluster initial mass function had remained unaffected (above the fading line), the ratio between the number of clusters with masses $3\times10^4\mathrm{M}_\odot \leq$ m $\leq 3\times10^5\mathrm{M}_\odot (4.5 \leq \log m/\mathrm{M}_\odot \leq 5.5)$ and the number of clusters with masses $3\times10^5\mathrm{M}_\odot \leq m \leq 10^6\mathrm{M}_\odot (5.5 \leq \log m/\mathrm{M}_\odot \leq 6)$ would be

$$\frac{\int_{0.03}^{0.3} m^{-2}\mathrm{d}m}{\int_{0.3}^{1} m^{-2}\mathrm{d}m} \simeq 13\,. \qquad (11)$$

To make use of the solar metallicity model raises the fading line by $\log m \simeq 0.3$ at most in the $\log m$ vs $\log t$ plot through an increase of the metallicity dependent mass-to-light ratio. This therefore leads to a decrease in the number of detectable clusters whose mass is lower than $3\times10^5\,\mathrm{M}_\odot$. Even in that case however, the proportion between the number of high-mass clusters ($5.5 \leq \log m/\mathrm{M}_\odot \leq 6$) and the number of lower-mass clusters (i.e. clusters whose mass is larger than the solar metallicity fading line and lower than $3\times10^5\mathrm{M}_\odot$) is still $\simeq 6.5$. There is an obvious discrepancy between these theoretical ratios, whatever the metallicity of the fading line, and the observed ratios as the majority of the clusters in the pre-burst phase have masses greater than $3\times10^5\mathrm{M}_\odot$. We emphasize here that the mass error bars do not affect this outcome significantly. For instance, let us consider the old and high-mass cluster, B1-36 ($\log t = 10.$, $\log m/\mathrm{M}_\odot = 5.91$; see Table 1). The rather large mass error bar suggest that its mass may be as low as $\log m/\mathrm{M}_\odot = 4.86$, so that it may contribute to the low-mass clusters of the pre-burst phase. However, its age and its mass errors are strongly correlated through the age-dependent mass-to-light ratio, that is, the lower mass limit is coupled with the lower age limit ($\log t = 8.6$) and not with the best age estimate (see Sect. 4.2). As a result, the high-mass clusters whose minimal estimate is lower than $\log m/\mathrm{M}_\odot = 5.5$ are not expected to contribute to the low-mass clusters class of the pre-burst phase.

The depletion in low-mass clusters at intermediate age shown by Fig. 8 is a real effect and illustrates the dynamical evolution of the M82 B cluster system. The disruptive processes working on time-scales on the order of a Hubble time include the tidal interactions between the clusters and the gravitational field of the parent galaxy and the evaporation through two-body relaxation within clusters, the latter being enhanced by the former. They affect mostly the low-mass clusters (e.g. Gnedin & Ostriker 1997, de Grijs et al. 2002). The detection of such evolutionary effects is not unexpected because of the dense environment achieved in this fossil starburst of the low-mass galaxy M82. A similar cluster disruption time-scale was derived in the dense centre of the massive spiral M51 (Boutloukos & Lamers 2002). Furthermore, de Grijs et al. (2002) show that the mean densities in M82 B and in the centre of M51 are remarkably

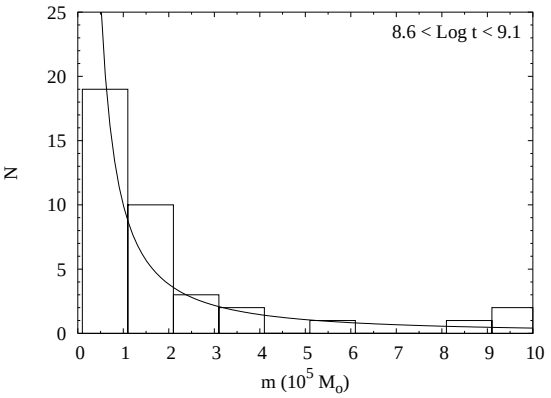

Figure 9. Mass histograms of the star clusters ($8.5< \log t/\mathrm{yr} < 9.1$) in the whole M82 B region and, overplotted, the best-fitting power-law. SSCs whose B, V, I is either an upper or lower limit have been ignored

similar, within an order magnitude. This therefore suggests that cluster disruption time-scales are primarily driven by the density of the environment in which the clusters are embedded, irrespective of the mass of the host galaxy. Such a result is not unexpected. The cluster stars which venture to large enough distance from the cluster centre are stripped off due to the tidal influence of the host galaxy, leading to a cluster which is tidally truncated at a finite tidal radius r_t given by:

$$r_t = R\left(\frac{m}{3M_{\mathrm{gal}}}\right)^{1/3}, \qquad (12)$$

where R is the galactocentric distance of the cluster and M_{gal} is the mass of the galaxy within R. Equation (12) also implies that the density of a GC, ρ_{cl}, cannot be less than three times the average density of the host galaxy inside R, ρ_{gal}, that is $\rho_{\mathrm{cl}} \geq 3\rho_{\mathrm{gal}}$. If its orbital motion drives the cluster towards higher density regions of the host galaxy, the corresponding shrinkage of the cluster tidal radius causes a runaway tidal stripping of the outer cluster stars, thus decreasing the cluster mass and making it even more sensitive to the galactic tidal field. Ultimately, this may lead to the cluster's disruption.

Even in the Magellanic Clouds (MCs), which constitute environments dynamically and tidally more gentle than M82 B and M51, do low-mass clusters dissolve with time through normal internal process. Due to the smaller ambient density, the time-scale for depleting low-mass clusters is not that short in the MCs however: clusters with masses between 10^4 and $10^5\,M_\odot$ survive for a few Gyr (Elson & Fall 1985b, 1988, Mackey & Gilmore 2002a,b), which is not the case in M82 B. In the next section, we show that the depletion of low-mass clusters in M82 B is already at work at the burst time.

4.6 Mass functions

Figure 9 displays the cluster mass functions for B1 and B2 combined. We have considered the clusters with ages 8.6 $< \log t/\mathrm{yr} <$ 9.1. To include older clusters in our sample would artificially bias the cluster mass function towards higher masses because of the dynamical destruction with

time of the low-mass clusters. De Grijs et al. (2002) derive a characteristic cluster disruption time-scale for the M82 B cluster system of $\log(t_{\rm dis}/{\rm yr}) \simeq 7.5 + 0.62 \times \log(m/10^4\,{\rm M}_\odot)$. Obviously, the dynamical destruction of star clusters in M82 B takes place on very short time-scales. In fact, the disruption time-scale in M82 B is the shortest known in any disc (region of a) galaxy. Considering the clusters formed at $\log t/{\rm yr} = 8.6$, the relation between the disruption time-scale and the cluster mass mentioned above shows that significant disruption must have already affected clusters with masses below $5.9 \times 10^5\,{\rm M}_\odot$. For the clusters formed at $\log t/{\rm yr}$=9.1 (i.e. almost at the onset of the burst), the same relation indicates that the upper mass of the clusters significantly affected by disruption is even greater, i.e. $3.8 \times 10^6\,{\rm M}_\odot$. Thus, the dynamical destruction processes have strongly altered the whole range of the initial mass function of the M82 B clusters with ages $8.6 < \log t/{\rm yr} < 9.1$. As a result, the current mass spectrum of these clusters (see Fig. 9) no longer represents the formation conditions of the cluster system.

In galaxies hosting systems of young clusters for which deep *HST* observations are available, the cluster luminosity functions do not show strong evidence for any turnover. In fact, their shape is consistent, down to the completeness threshold, with a decreasing power-law of the form $\phi(L){\rm d}L \propto L^\alpha {\rm d}L$, where $\phi(L){\rm d}L$ is the number of young star clusters with luminosities between L and $L + {\rm d}L$ and α is the slope of the cluster luminosity function. Since in the age range we consider, i.e. $8.6 < \log t/{\rm yr} < 9.1$, the mass-to-light ratio does not vary significantly with time and metallicity ($m/L_V \simeq 1$), we can directly compare the mass function shown in Fig. 9 with the luminosity functions derived for other young star cluster systems in merging galaxies or merger remnants (e.g. NGC 4038/4039, $\phi(L) \propto L^{-1.8}$, Whitmore & Schweizer 1995; NGC 3256, $\phi(L) \propto L^{-1.8}$, Zepf et al. 1999; NGC 3921, $\phi(L) \propto L^{-2.1}$, Schweizer et al. 1996; NGC 7252, $\phi(L) \propto L^{-1.8}$, Miller et al. 1997; NGC 3610, $\phi(L) \propto L^{-1.9}$, Whitmore et al. 2002). We have estimated the best-fitting power-law exponent with the Levenberg-Marquardt method (Press et al. 1997). The mass function in Fig. 9 follows ${\rm d}N \propto m^{-1.4\pm0.2}{\rm d}m$ (see also de Grijs et al. 2001). Our slope is therefore shallower than what has been found for many other young star cluster systems and shows better agreement with the luminosity function of the young star cluster population in the Large Magellanic Cloud ($\alpha = -1.5 \pm 0.2$, Elson & Fall 1985a). The most likely cause for such a rather shallow slope is the short disruption time-scale of the M82 B cluster system. The clusters first affected by the disruption are the lowest-mass ones, even though the most massive clusters formed at the time of the burst have already gone through significant disruption processes too. Due to the shorter disruption time-scale, any initial mass function will get biased towards higher masses as time goes on and an initial steep slope will turn into a shallower one. Moreover, the mass distribution of the clusters formed during the burst shows a turnover at $\log m/M_\odot \simeq 5.3$ (de Grijs et al. 2002), not caused by selection effects (see the location of the fading line in Fig. 8). This also contributes to the difference in slope.

5 CONCLUSIONS

We have estimated the age, the metallicity and the mass of 87 clusters located in M82 B, a fossil starburst site in the irregular galaxy M82. Since this galaxy is located outside the Local Group, our analysis is based on spectral synthesis models. We have compared the *HST* $BVIJ$ photometry obtained by de Grijs et al.(2001) with the colours of simple stellar populations (Bruzual & Charlot 1996). Because the isochrones and the iso-metallicity tracks are not parallel in a $(V-I)_0$ vs $(V-J)_0$ plot, we have been able to lift the age-metallicity degeneracy.

Our results have confirmed the peak in the cluster formation rate detected by de Grijs et al. (2001). From 1.5 to 0.5 Gyr ago, as M82 was getting closer to its large spiral companion M81, M82 B went through a period of enhanced cluster formation, most probably induced by the increasing tidal interactions. We have emphasized its chemical evolution showing that M82 B underwent a chemical enrichment phase up to super-solar metallicities (i.e. Z> $Z_\odot$) about 1 Gyr ago. The stellar ejecta from older stellar populations have most probably enriched the interstellar medium out of which the 1 Gyr old clusters formed. At almost the same time however, a subpopulation of very metal-poor clusters formed in B2, i.e. the part of M82 B nearest the galactic centre. Their formation may have been stimulated by infall, onto B2, of "fresh" circumgalactic gas which had escaped the chemical enrichment of the interstellar medium while orbiting M82. The clusters in B1, the eastern part of M82 B, may have been self-enriched at the time of their formation since they show a mass-metallicity correlation in the sense expected by simple self-enrichment models applied to pressure-truncated clouds. In B2 however, a clear-cut relation does not show up. Due to the infall of circumgalactic gas, the pressure may not have been stable enough to allow the formation of pressure-bound clouds. The eastern (B1) and western (B2) parts of M82 B are therefore different with respect to both the mass-metallicity diagrams and the formation of very metal-poor clusters at the time of the burst. We have also highlighted the dynamical destruction of the low-mass clusters over time-scales of the order of several 10^7yr. Finally, we have shown that the mass function of the clusters in a given age range obeys a power-law as observed for many cluster systems formed in merging galaxies. However, the slope of the mass function of cluster systems associated with mergers is significantly steeper ($\alpha \simeq -2$) than the slope of the $\simeq 1$ Gyr old clusters in M82 B ($\alpha \simeq -1.4$). This is most likely due to the disruption processes at work in the M82 B region. Since the low-mass clusters are more quickly destroyed, the mass function will get biased towards higher masses and a steep initial mass function will turn into a shallower one.

ACKNOWLEDGMENTS

G.P. warmly thanks the Cambridge Institute of Astronomy for its hospitality where much of this work was carried out. This research was supported by the European Community under grant HPMT-CT-2000-00132. G.P. is grateful to P. Magain (Liège Institute) for fruitful advices when tackling the issue of the error propagation.

REFERENCES

Bik A., Lamers H.J.G.L.M., Bastian N., Panagia N., Romaniello M., Kirshner R., 2002, A&A, in press (astro-ph/0210594)

Brouillet N., Baudry A., Combes F., Kaufman M., Bash F., 1991, A&A, 242, 35

Boutloukos S.G., Lamers H.J.G.L.M., 2002, MNRAS, in press (astro-ph/0210595)

Bruzual G., Charlot S., 1996, in: Leitherer C., et al., 1996, PASP, 108, 996 (AAS CDROM Series 7) (BC96)

Cardelli J.A., Clayton G.C., Mathis J.S., 1989, ApJ, 345, 245

de Grijs R., 2001, A&G, 42, 14

de Grijs R., O'Connel R.W., Gallagher J.S. III, 2001, AJ, 121, 768

de Grijs R., Bastian N., Lamers H.J.G.L.M., 2003, MNRAS, in press (astro-ph/0211420)

Elson R.A.W., Fall S.M., 1985a, PASP, 97, 692

Elson R.A.W., Fall S.M., 1985b, ApJ, 299, 211

Elson R.A.W., Fall S.M., 1988, AJ, 96, 1383

Fall S.M., Rees M.J., 1985, ApJ, 298, 18

Freedman W. et al., 1994, ApJ, 427, 628

Gnedin O.Y., Ostriker J.P., 1997, ApJ, 474, 223

Holtzmann J.A., Watson A.M., Mould J.R., Gallagher J.S. III, Ballester G.E., Burrows C.J., Clarke J.T., Crisp D., Evans R.W., Griffiths R.E., Hester J.J., Hoessel J.G., Scowen P.A., Stapelfeldt K.R., Trauger J.T., Westphal J.A., 1996, AJ, 112, 534

Kroupa P., Tout C.A.& Gilmore G.F., 1993, MNRAS, 262, 545

Larson B.L., 1998, MNRAS, 301, 569

Mackey A.D., Gilmore G.F., 2002, MNRAS, accepted for publication

Mackey A.D., Gilmore G.F., 2002, in:"New Horizons in Globular Cluster Astronomy", ASP Conf. Series, 2002, eds G. Piotto, G. Meylan, G. Djorgovski, M. Riello

Marcum P., O'Connell R.W., 1996, in From Stars to Galaxies: The Impact of Stellar Physics on Galaxy Evolution, eds. C. Leitherer, U. Fritze-von Alvensleben, J. Huchra (San Francisco: ASP), 419

McLaughlin D.E., Pudritz R.E., 1996, ApJ, 469, 194

Meylan G., Heggie D.C., 1997, A&AR, 8, 1

Miller B.W., Whitmore B.C., Schweizer F., Fall S.M., 1997, AJ, 114, 2381

O'Connell R.W., Mangano J.J., 1978, ApJ, 221, 62

O'Connell R.W., Gallagher J.S., Hunter D.A. Colley W.N., 1995, ApJ, 446, L1

Parmentier G., Jehin E., Magain P., Neuforge C., Noels A., Thoul A., 1999, A&A, 352, 138

Parmentier G., Gilmore G., 2001, A&A, 378, 97

Press W.H., Teukolsky S.A., Vetterling W.T. and Flannery B.P. 1997, Numerical Recipes (2nd ed.; Cambridge Univ. Press)

Pryor C., Meylan G. 1993, In: S.G. Djorgovski, G. Meylan (eds) ASP Conference Series Volume 50, Structure and Dynamics of globular clusters, p. 370

Rieke G.H., Loken K., Rieke M.J., Tamblyn P., 1993, ApJ, 412, 99

Rosenberg A., Saviane I., Piotto G., Aparicio A., 1999, AJ, 118, 2306

Satyapal S., Watson D.M., Pipher J.L., Forrest, W.J. Forrest W.J., Greenhouse M.A., Smith H.A., Fischer J., Woodward C.E., 1997, ApJ 483, 148

Searle L., Sargent W.L.W., Bagnuolo W.G., 1973, ApJ, 179, 427

Schweizer F., Miller B.W., Whitmore B.C., Fall S.M., 1996, AJ, 112, 1839

Shen J., Lo K.Y., 1995, ApJ, 445, L99

Tinsley B.M., 1972, A&A, 20, 383

Whitmore B.C., Schweizer F., 1995, AJ, 109, 960

Whitmore B.C., Zhang Q., Leitherer C., Fall M., Schweizer F., Miller B.W., 1999, AJ, 118, 1551

Whitmore B.C., Schweizer F., Kundu A., Miller B.W., 2002, AJ, 124, 147

Wills K.A., Das M., Pedlar A., Muxlow T.B.W., Robinson T.G., 2000, MNRAS, 316, 33

Worthey G., 1994, ApJS, 95, 107

Yun M.S., Ho P.T.P., Lo K.Y., 1994, Nat., 372, 530

Zepf S.E., Ashman K.M., English J., Freeman K.C., Sharples R.M., 1999, AJ, 118, 752

Zhang Q., Fall S.M., Whitmore B.C., 2001, ApJ, 561, 727